Journal of the American Ceramic Society

RESEARCH ARTICLE OPEN ACCESS

In Situ Raman Spectroscopy of a Silica Gel-Templated Hydration Pathway in CO_2-Activated Cement

Marcin Hajduczek[1] | Yogiraj Sargam[2] | Sean Monkman[3] | Vishnu Chaudhari[3] | Santiago El Awad[1] | Franz-Josef Ulm[1] | Admir Masic[1]

[1]Department of Civil and Environmental Engineering, Massachusetts Institute of Technology, Cambridge, Massachusetts, USA | [2]Indian Institute of Technology Jodhpur, Jodhpur, Rajasthan, India | [3]CarbonCure Technologies, Dartmouth, Canada

Correspondence: Admir Masic (masic@mit.edu)

Received: 1 December 2025 | **Revised:** 2 April 2026 | **Accepted:** 4 May 2026

Keywords: $CaCO_3$ | cement hydration | in situ CO_2 mineralization | Raman microspectroscopy | silica gel

ABSTRACT

This study investigates early-age carbonate mineralization in cementitious systems using in situ Raman microspectroscopy. In the presence of dissolved CO_2, clinker phases undergo accelerated dissolution, decomposing to form various calcium carbonate polymorphs and a transient amorphous silica gel network. Once the available CO_2 is consumed, clinker hydration resumes, leading to delayed calcium–silicate–hydrate (C–S–H) and portlandite ($Ca(OH)_2$) formation. The precipitation of portlandite through the pore network triggers a localized pozzolanic reaction at the silica gel–portlandite interface, yielding a distinct calcium–silicate–hydrate (C–S–H*). This templated mechanism produces a homogeneous and highly polymerized binder, leading to improved 24-h compressive strength compared to reference samples. Correlation function analysis confirms that the evolution of silica gel, portlandite, and C–S–H follows a three-stage sequence—*mineralization*, *transition*, and *stabilization*—quantitatively demonstrating a strong spatial anticorrelation between silica gel dissolution and portlandite precipitation. These findings establish a new chemomechanical framework for CO_2 mineralization in cement, highlighting transient silica gel as a critical intermediate for engineering sustainable, high-performance concrete.

1 | Introduction

Concrete, a cement-based composite, is the most widely used construction material globally, valued for its excellent versatility, production from locally available raw materials, low cost, and inherent resistance to water, fire, and cyclic loading [1]. On a unit-mass basis, concrete has the lowest carbon footprint compared to other major construction materials such as glass, steel, and wood [2]. However, the enormous scale of concrete production—around 30 Gt annually—is associated with approximately 8% of global anthropogenic GHG emissions and 3% of global energy demand [3], driven mainly by the carbon footprint of cement.

Recognizing this challenge, global organizations such as CEMBUREAU, Portland Concrete Association (PCA), and the Global Cement and Concrete Association (GCCA) have published 2050 net-zero roadmaps [4–7]. These roadmaps highlight strategies to be implemented across the cement and concrete value chain, such as mix design optimization, energy efficiency improvements, renewable fuel adoption, and increased use of recycled materials. Importantly, they emphasize a role for carbon capture, utilization, and storage (CCUS) technologies which, in the GCCA roadmap, for example, is expected to contribute 36%–40% of the required emission reductions by 2050 [6]. Within the CCUS framework, carbon dioxide (CO_2) utilization and mineralization in concrete has emerged as a promising solution. Numerous studies [8–10] have examined its scalability, carbon-reduction potential, and economic viability. A recent analysis by Driver et al. [11] estimated that competitive CO_2 mineralization technologies could abate up to 0.39 Gt CO_2-eq annually—equivalent to ~15%

of the cement-sector emissions in 2020—with this potential expected to grow significantly in the coming decades.

One approach for CCUS within the cement and concrete value chain is the use of CO_2 as an admixture in fresh concrete, where it reacts with cementitious phases to form stable carbonate products. The injected CO_2 dissolves in water to form carbonic acid (H_2CO_3), which rapidly deprotonates in the highly alkaline environment into carbonate ions (CO_3^{2-}). The carbonate ions then combine with the Ca^{2+} ions present in the pore solution to undergo a mineralization reaction. The overall activation of the silicate clinker phases with CO_2 (Equations 1 and 2) to form coproducts of a calcium–silicate–hydrate (C–S–H) gel and calcium carbonate was first described by Young et al. [12].

$$2CaO \cdot SiO_2 + (2-x)\,CO_2 + yH_2O \rightarrow xCaO \cdot SiO_2 \cdot yH_2O + (2-x)\,CaCO_3 \quad (1)$$

$$3CaO \cdot SiO_2 + (3-x)\,CO_2 + yH_2O \rightarrow xCaO \cdot SiO_2 \cdot yH_2O + (3-x)\,CaCO_3 \quad (2)$$

Precipitation of nanoscale (~70 nm) calcium carbonate particles occurs rapidly, as early as within 60 s of injection [13–15]. The earliest precipitates are typically amorphous or poorly crystalline. Investigations on model tricalcium silicate (or C_3S in cement chemistry notation) systems [13, 15] further revealed that CO_2 injection rapidly alters early hydration: fibrous C–S–H and carbonate precipitates form almost simultaneously, while accelerated Ca^{2+} removal induces undersaturation, enhancing the rate of C_3S dissolution. Importantly, although carbonate and C–S–H develop in parallel, evidence suggests that carbonate may not act as a direct nucleation site for C–S–H but can be subsequently encapsulated within the growing gel [16, 17].

Unlike intentional CO_2 injection during mixing, which can promote beneficial mineralization, the long-term carbonation of conventional hardened concrete represents a pervasive degradation process [18]. It begins with the diffusion of atmospheric CO_2 into the pore network, where it reacts with existing hydration products to alter the mature binder structure. Over time, this continued late-stage carbonation lowers the pore solution pH, while concurrently decalcifying C–S–H and forming amorphous silica gel which compromises concrete's strength and durability [19–21]. In contrast, when CO_2 is introduced during initial mixing, it interacts directly with dissolving clinker phases before the primary binder network is established. This allows for the precipitation of carbonate products alongside the developing binder rather than at the expense of traditional hydration products.

It is worth noting that a significant gap exists in understanding the chemical evolution and stability of the early-age hydration products and carbonate phases formed during activation of cement with CO_2. Due to the inherent limitations of conventional analytical and microscopic techniques, many prior investigations into CO_2 mineralization in cementitious systems have relied on theoretical interpretations rather than direct experimental evidence. For example, Sargam et al. suggested that the C–S–H gel formed under CO_2 injection may possess distinct mechanical properties compared to the gel produced under normal hydration conditions [17]. Similarly, it has been hypothesized that the precipitated carbonate and the C–S–H gel may form an intermixed composite phase. However, such interactions remain unconfirmed, as direct visualization has proven challenging. In SEM and TEM analyses, carbonate particles are typically observed to be rapidly and completely encapsulated by the growing gel, which makes it difficult to resolve intermixed domains within the limited interaction volumes of these techniques [14].

The lack of direct experimental validation has left fundamental mechanistic questions unanswered—particularly regarding whether CO_2 injection alters the conventional cement hydration pathway, and how carbonate formation interacts with unhydrated clinker and hydrated phases. Solid-state nuclear magnetic resonance (NMR) studies have provided invaluable insights into the silicate chain structure of C–S–H under normal hydration conditions [19]. However, the application of such techniques to systems undergoing rapid carbon mineralization is challenging. Raman spectroscopy has emerged as a powerful technique for the in situ study of cement hydration and carbonation processes due to its molecular specificity, minimal sample preparation requirements, and ability to provide spatial resolution at the micron scale [20, 21]. Unlike X-ray diffraction, which is highly effective for crystalline phases, Raman spectroscopy can detect poorly crystalline and amorphous phases, making it particularly suited for analyzing early-age hydration products like C–S–H gel, sulfate-containing phases, and various carbonate polymorphs [16, 22]. The technique operates by measuring the inelastic scattering of light, providing a vibrational fingerprint that can be assigned to specific molecular groups and symmetries [23]. In the context of carbonation, confocal Raman microscopy (CRM) is exceptionally valuable for identifying and distinguishing between the various polymorphs and amorphous phases of calcium carbonate (calcite, vaterite, aragonite, amorphous calcium carbonate) based on their characteristic lattice modes and internal vibrational modes [24]. This makes it possible to map the distribution of carbonation products within a fresh sample and track polymorphic transformations over time [16]. Furthermore, the chemical evolution of the silicate groups within the cement paste can be monitored through changes in the Si–O–Si stretching (~400–700 cm^{-1}) and bending (~1000–1200 cm^{-1}) bands [25].

This study examines the early-age (first 24 h) carbon mineralization in oilwell cementitious systems utilizing in situ CRM. In the presence of dissolved CO_2, clinker phases experience enhanced dissolution, resulting in the formation of various calcium carbonate polymorphs and amorphous silica gel. Upon complete consumption of the introduced CO_2, the conventional hydration of clinker resumes, resulting in the formation of portlandite and additional C–S–H.

2 | Experimental Methods

2.1 | Cement Material

The experimental work employed an API Spec 10A Class G (oilwell) cement, chosen for its lower calcite content compared to ASTM Type I (ordinary Portland) or Type IL (Portland–limestone) cements. Its reduced carbonate content (as indicated by a low loss on ignition or LOI) makes it particularly suitable

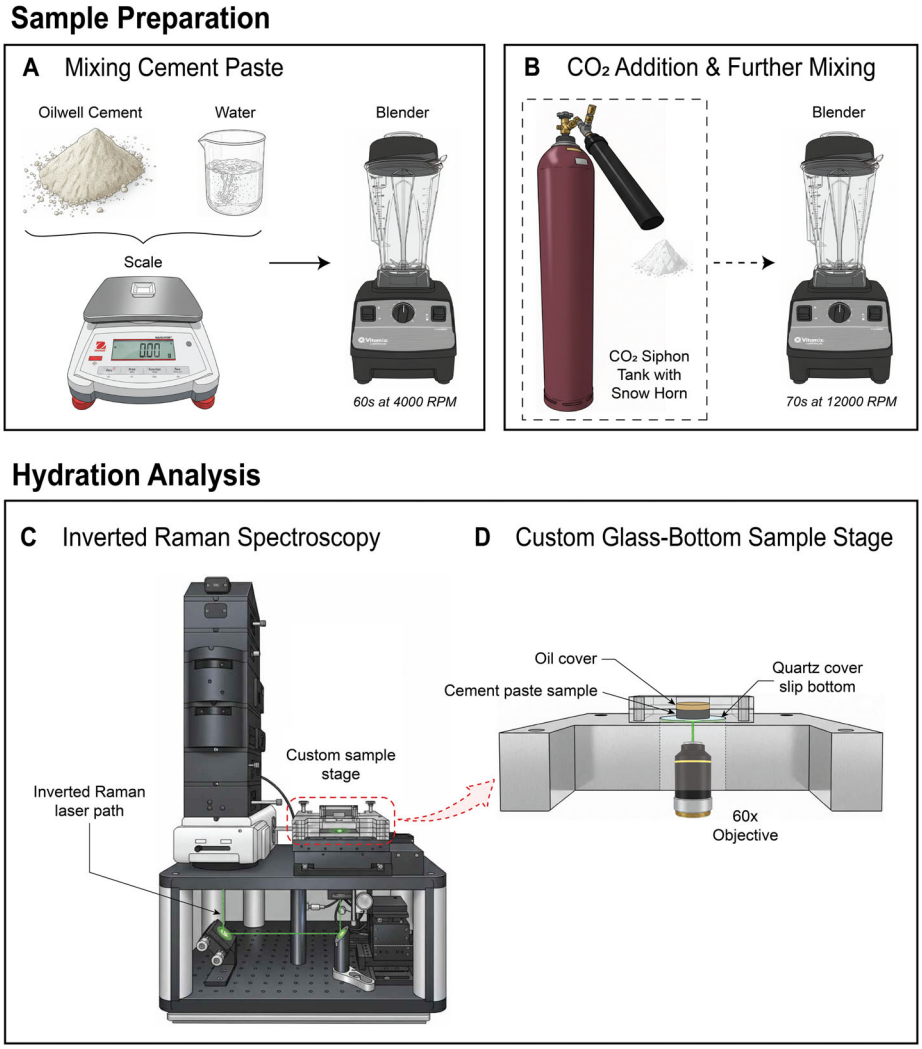

FIGURE 1 | Lab approach for preparing and analyzing cement paste samples with injected CO_2. (A) Cement and water were mixed at a 1.0 w/c ratio for 60 s. (B) A CO_2 siphon tank fitted with a snow horn was used to produce solid CO_2 flakes, which were then added to the cement paste in the CO_2-activated samples, followed by additional mixing at higher speeds. (C) Confocal Raman spectroscopy setup for in situ cement CO_2 mineralization imaging, utilizing an inverted beam path to acquire data from below the sample stage. (D) Custom-fabricated sample stage incorporating a quartz window base. Cement paste hydrates while pressed directly over the window, allowing for Raman scanning from below. A thin oil cover over the sample prevents interaction with atmospheric CO_2.

for observing, measuring, and quantifying the formation of low-abundance carbonate reaction products [26]. Class G cements have lower alkalis and SO_3 compared to Type I and IL cements. The chemical composition and phase assemblage of the cement is reported in Table S1.

Although Type G offers a simplified platform for mechanistic study, translating these insights to conventional systems—including Type I, Type IL, and mixtures incorporating SCMs—is necessary to evaluate their broader applicability. Because hydration phase assemblages are strongly influenced by SCMs [27, 28] the present study should be viewed as a foundation for such translation.

2.2 | Cement Paste Sample Preparation for CRM

The cement paste was prepared by mixing equal parts (by mass) of cement and deionized water (w/c ratio of 1.0) using a variable-speed Vitamix blender. The paste was first mixed for 30 s at 4000 RPM, then scraped off the sides of the mixer to ensure consistency before being mixed for another 30 s at the same speed (Figure 1A). The second step of mixing (Figure 1B) was conducted at 12000 RPM for 30 s, after which mixing was again paused to scrape the sides of the mixer. Finally, the paste was mixed a final time at 12000 RPM for 40 s.

For CO_2-injected samples, solid CO_2 powder was added to the mixer before the final 40 s of mixing. The CO_2 was obtained from a CO_2 siphon tank fitted with a snow horn apparatus to its CGA-320 valve (Figure 1B). The snow horn rapidly depressurizes the liquid CO_2 in the tank, resulting in a sudden volumetric expansion and cooling that instantly freezes the released carbon dioxide into solid CO_2 "flakes." This powder can be readily mixed and homogeneously dispersed into the cement paste without additional processing. Upon contact with the aqueous paste during mixing, the solid CO_2 flakes rapidly sublimate into CO_2 gas. A portion of this CO_2 immediately dissolves into the pore

solution, while the remainder fills the mixer's headspace and subsequently dissolves as mixing proceeds.

Once mixed, the slurry-like paste was extracted from the blender and placed into the cylindrical well of the custom-fabricated Raman stage detailed in Figure 1D. The resulting sample, measuring 0.5 in. in diameter and 0.25 in. in height, was then quickly covered with a thin layer of vegetable oil to prevent evaporation of pore water and interaction with atmospheric CO_2 over long scan times. The custom stage was then mounted into a Raman spectroscope, allowing for acquisition of chemical data within minutes of mixing (Figure 1C).

2.3 | Confocal Raman Spectroscopy

A WITec Alpha 300RA Confocal Raman Microscope (CRM) was used to obtain Raman spectra from 0 to 24 h of hydration in this study. The system was equipped with an Nd:YAG laser with a wavelength (λ) of 532 nm, and a CCD camera cooled to −60°C for quantifying the intensity of Raman spectra. A silicon wafer standard with a known Raman spectrum was used to calibrate the device's excitation wavelength. A 60× Zeiss objective was used in an inverted microscopy setup, as detailed in Section 3.1 (Figure 1). In all tests, Raman maps were acquired across 100 μm × 100 μm scan areas (100 × 100 points) with a continuous laser beam and an accumulation time of 0.3 s per point, resulting in one map per hour of hydration. The same scan area was continuously scanned for 24 h, resulting in 24 Raman maps that tracked early stage hydration and carbonation reactions. It should be noted that because the acquisition of a single map occurs via continuous point-by-point raster scanning over the course of an hour, there is a temporal difference of approximately 60 min between the top and bottom of a single scan. Given the rapid kinetics of early hydration, this means that a single Raman map may capture evolving phases. At least three samples were tested via Raman mapping at each CO_2 dosage (0% reference, 0.1%, 0.3%, and 1.0% CO_2 injection) to ensure results were representative of the entire sample, as cementitious materials are intrinsically heterogeneous.

Raman data were processed using WITec Project and MATLAB software for analysis and visualization. To mitigate the background fluorescence inherent to early-age cementitious systems, particularly at low wavenumbers, data acquisition was performed utilizing the WITec system's integrated fluorescence filter. All collected spectra were first cropped and processed with polynomial background subtraction to flatten baseline drift, filter out residual noise and increase spectral resolution. Three separate techniques were employed to analyze the resulting data: basis analysis, average spectral analysis, and peak evolution analysis. Basis spectra of individual components in the cementitious matrix were computed using the true component analysis, cluster analysis, and demixing functions in WITec Project Five software. Average Raman spectra were obtained by averaging the intensity of each wavenumber in the spectrum at every point in the scan area (100 μm × 100 μm scans, with 1 point/μm^2). With data collected across the entire scan area once per hour, the average spectrum shows the general peak profiles at each time step. Finally, a MATLAB script was devised to track the evolution of the CH and silica gel peaks in the average spectra by fitting each peak with a Gaussian distribution and deconvoluting their overlapping intensities.

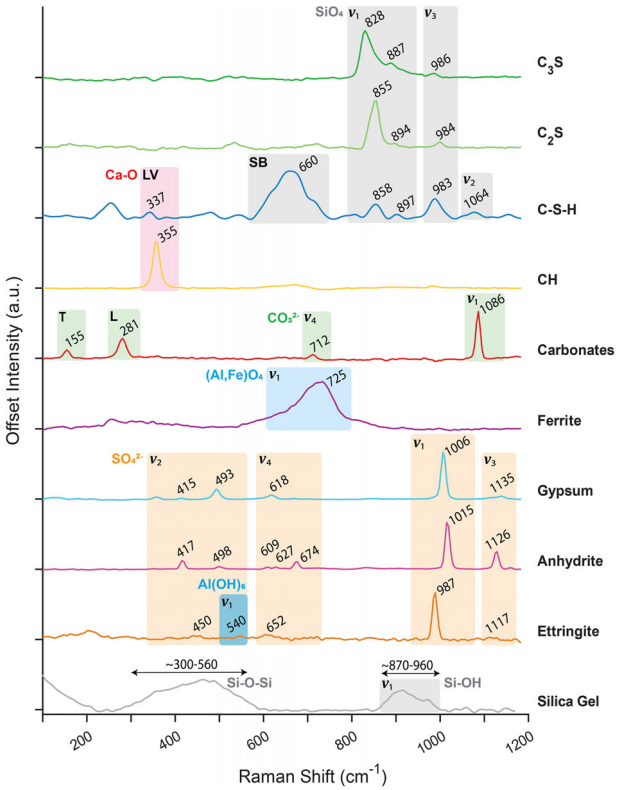

FIGURE 2 | Basis Raman spectra of individual phases in the cement system, with characteristic peak positions labeled. Key vibrational modes are color-coded according to their corresponding chemical group.

For quantitative correlation function analysis, Raman phase distribution maps were generated using a spectral filter within the WITec software to identify local signal maxima within specific wavenumber regions. These regions correspond directly to the characteristic bands of the basis spectra shown in Figure 2. Because the confocal interaction volume frequently captures mixed phases within a single pixel, intensity thresholds for phase color-coding were determined via visual inspection to ensure each target phase was definitively observable above the localized background signal.

2.4 | Isothermal Calorimetry

Cement hydration kinetics were characterized using a TAM Air isothermal calorimeter (TA Instruments, Georgia, USA) operating at 22°C with continuous monitoring over 72 h. For each system, two replicates were prepared with a total sample volume of 15 cm^3 per replicate, each paired with a reference vial containing water of equivalent heat capacity. Samples were mixed externally using a high-shear blender (as outlined in Figure 1) and transferred into the calorimeter. Data collected prior to thermal equilibrium—reflecting disturbances introduced by opening the calorimeter for sample loading—were discarded from the analysis. Heat flow rate ($\dot{Q}(t)$) and cumulative heat ($Q(t)$) were obtained by normalizing the calorimetric signal to the cement mass in each vial. Three distinct thermal markers

[29, 30] for onset time were determined using the open-source Python calorimetry package CaloCem [29]: the end of the induction stage (t_{is}), the maximum slope of the acceleration stage (t_m), and the time to reach the peak heat flow $\dot{Q}_{max}(t_{max})$.

2.5 | Pore Solution pH Measurements

The alkalinity of the pore solution during early-stage hydration was measured for both the reference and 1% CO_2 systems using a Hanna edge Dedicated digital pH meter (Hanna Instruments, Rhode Island, USA) equipped with a glass electrode. Samples were prepared as for Raman spectroscopy (Figure 1A,B) and left to hydrate in sealed glass containers to avoid atmospheric contamination. Pore solution was extracted from the hydrating paste using a vacuum filtration assembly equipped with a Büchner funnel and a 0.45 μm polyvinylidene fluoride (PVDF) membrane filter. At designated hydration intervals (30 min, 1 h, 3 h, 5 h, 7 h, and 10 h), approximately 60 g of the hydrating paste was transferred to the funnel. A vacuum was applied until the onset of surface cracking of the filter cake (hydrated solids), yielding approximately 20–30 mL of filtrate for immediate chemical analysis. pH measurements were recorded upon reaching a steady-state response, typically within 90–120 s of immersing the electrode into the pore solution.

2.6 | Vicat Needle Penetration Testing

Preliminary data on the setting time of 1% CO_2 and reference samples were obtained using a manual Vicat apparatus fitted with a 1 mm needle according to ASTM C191 [31]. Cement paste samples were prepared in the same manner as for Raman spectroscopy, except in larger quantities to fill the standard conical ring mold used for testing (60 mm diameter and 40 mm height). Immediately after casting, both 1% CO_2 and reference samples were tested by setting the Vicat needle to the surface of the paste, allowing it to penetrate the sample under gravitational self-weight, and recording the resulting penetration depth. This procedure was repeated every 15 min for the first 24 h of hydration, with three tests conducted at each time step to ensure reliability of the data. Samples were kept in a humid chamber between tests. In accordance with ASTM C191, pastes were considered to have reached *initial setting* when the needle's penetration depth was 25 mm (out of 40), and *final setting* once the needle did not penetrate the sample surface.

2.7 | Mortar Cube Mix Design

Mortar specimens were prepared using Class G cement and standard graded sand conforming to the specifications of EN 196-1 [32]. The mix proportions for the mortars, designed with water to cement (w/c) mass ratios of 1.0, are detailed in Table S3. The mixing procedure followed the standard ASTM C305 [33] and the CO_2 was added in the mix as an admixture adhering to ASTM C494 [34], utilizing a bench-top epicycle type mechanical mixer. The sand content was tripled for the mix portion for water to cement ratio 1.0 to address the high fluid nature of the mixture.

Immediately after mixing, the fresh mortar was cast into 50 mm (2-in.) cube molds. The specimens were compacted to minimize entrapped air and then stored in a humid environment for 24 h as per ASTM C109. The compressive strength testing was carried out in triplicate, and the mean compressive strength for each batch is presented in Figure S4.

3 | Results and Discussion

3.1 | Inverted Confocal Raman Microscopy for In Situ Monitoring of Carbonate Mineralization in Cement

In order to facilitate in situ and operando spectroscopic analysis of the first 24 h of hydration, samples in this study were prepared by adding up to 1% CO_2 flakes (wt% of cement) from a siphon tank to the cement paste during mixing, as highlighted in Figure 1 and detailed in Section 2. This not only effectively mimics industrial approaches to CCUS, but also allows for immediate analysis, as samples react with CO_2 instantly rather than over extended periods of CO_2 gas exposure (as in a climate chamber). Owing to the low levels of CO_2 addition studied in this work, minimizing both the intrinsic carbonate content of reference samples as well as interaction with atmospheric carbon was paramount. As such, API Spec 10A Class G cement was used in sample preparation for its innately low carbonate content (Table S1), and a custom CRM setup was developed to facilitate Raman analysis.

Cement hydration and carbonate mineralization are dynamic processes with rapidly evolving phases. In order to capture these phase transformations with Raman, relatively quick data acquisition is needed—especially for in situ monitoring—as well as high spatial and spectral resolution to map the distribution and chemical environments of different phases [21]. Simultaneously, a relatively low laser power (~1.5 mW) was required in the present work to prevent laser-induced sample alterations during 24-h periods of continuous scanning. To ensure the highest possible resolution despite low laser power and evolving hydration phases during acquisition times, a perfectly flat sample surface helps prevent loss of laser focus due to topographic differences.

Therefore, a custom-fabricated sample stage (Figure 1D) was used, in which samples were pressed flat against a quartz cover slip within a shallow cylindrical well. A thin layer of oil was added on top of the samples to prevent both the evaporation of pore water and, importantly, extraneous carbonation from atmospheric CO_2. Beneath the sample, the stage contained a central through-hole to accommodate the laser path from an inverted Raman spectroscopy setup (Figure 1C). This apparatus allowed for samples to be mounted in the CRM almost immediately after mixing, with data acquisition beginning within minutes of the start of hydration (following manual focusing of the laser objectives). Thereafter, in situ and operando cement monitoring proceeded via Raman spectroscopy of the same sample area over the course of 24 h. Section 2 outlines these sample preparation and spectroscopy procedures in more detail.

While analyzing cement pastes against a rigid barrier can create boundary effects that disrupt normal grain packing and artificially alter local porosity and hydration kinetics, the inverted spectroscopy setup used in this study helps mitigate these potential artifacts. By compacting the cement slurry against the

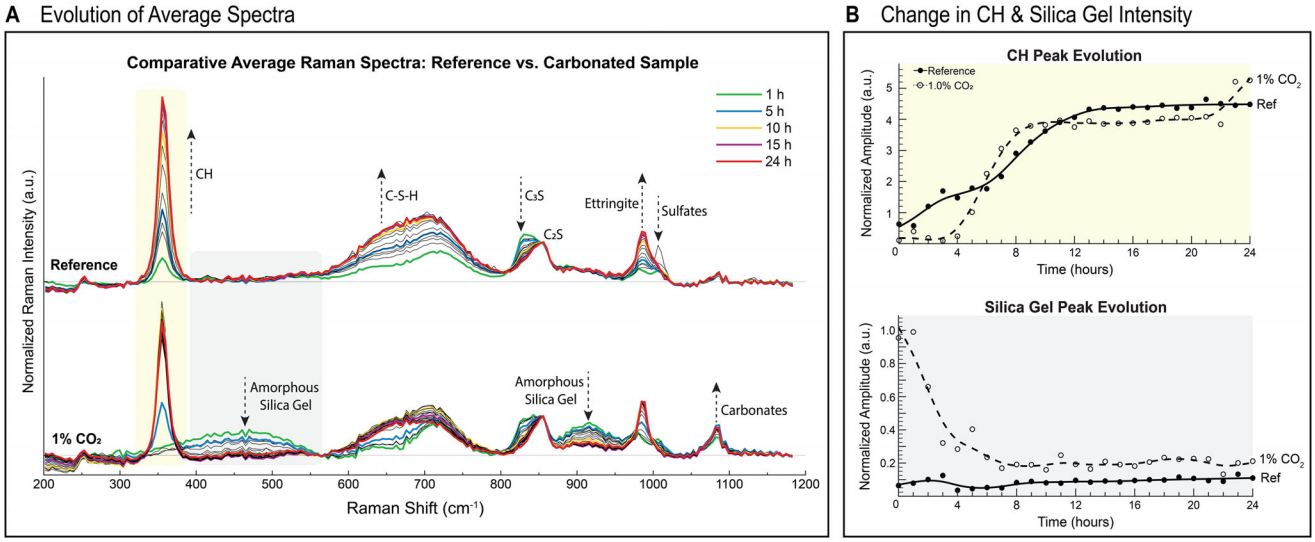

FIGURE 3 | Comparative Raman spectroscopy of cement hydration with and without CO_2. (A) Time-resolved average spectra of the reference and 1% CO_2 samples over 24 h. Each spectrum acts as a chemical "fingerprint" of the entire sample area at a specific point in time, with select time points highlighted to reveal the differing evolution of hydration and carbonation reaction products in reference and CO_2-activated samples. (B) Quantitative analysis of key Raman peak intensities extracted from average spectra. The plots track the average evolution of CH and silica gel from multiple replicate samples, comparing the reference condition to samples with 1.0% CO_2 addition by mass.

bottom quartz cover slip under its own self-weight, a flat, densely packed imaging surface was maintained throughout hydration. Furthermore, the CRM instrument's confocal depth resolution of 3 μm allowed for precise subsurface imaging. Specifically, the focal depth of the laser was positioned 4–5 μm past the quartz-paste interface to minimize surface contribution, yielding an analyzed volume approximately between 3 and 6 μm into the sample. This depth effectively minimizes physical boundary effects while remaining well within the optimal Raman signal range, as empirical profiling showed that the paste's inherent opacity does not completely attenuate the signal until a depth of ~21 μm.

3.2 | Early-Age CO_2 Mineralization

To elucidate the underlying chemomechanical changes that occur in hydration pathways of early-stage carbonate mineralization, three separate spectral analysis techniques were employed, akin to the Raman analysis framework outlined in prior work by Loh et al. [21]. First, basis spectra of individual components in the cementitious matrix were computed. Each cement phase (e.g., C_3S, CH, carbonates, etc.) was then identified by comparing the peaks in its computed basis spectrum to reference spectra from the literature, which showed excellent agreement barring small discrepancies from experimental conditions and equipment [20, 21, 24, 25, 35–41]. Figure 2 illustrates these resulting basis spectra, highlighting their characteristic peak locations and vibrational modes (see Supporting Information for more details). It is worth noting that the spectral peaks of crystalline materials, such as CH and carbonates, are characteristically sharp and narrow. In contrast, amorphous phases like C–S–H and silica gel produce broad spectral bands.

In practice, because cementitious materials are highly heterogeneous, the Raman spectrum of any one point on the sample is a superposition of multiple basis spectra corresponding to the various phases coexisting in the Raman laser's interaction volume. By tracking the distribution and intensity of these characteristic peaks within the spectra over time, the evolution of each chemical phase can be monitored.

Average spectral analysis, the second technique employed, provides a robust method for tracking these changes by averaging the intensity of each wavenumber in the spectrum at every point in the scan area. Figure 3A shows the time-resolved average spectra of both reference samples and those with 1% CO_2 addition over 24 h of hydration. Key peaks are labeled alongside arrows showing the direction of each phase's evolution in time. To correct for time-dependent signal intensity variations and allow for direct comparison between samples, the average spectra were normalized using the primary belite (C_2S) peak at 855 cm^{-1} as an internal standard. This approach is based on the assumption that belite remains chemically stable and does not hydrate significantly during the first 24 h of data acquisition.

By highlighting select time points (1 h, 5 h, 10 h, 15 h, and 24 h) in the average spectra, differences between the evolution of reference and CO_2-activated samples can be readily observed. As expected, the 1% CO_2 sample contains a significant carbonate peak at ~1086 cm^{-1} that is absent from the reference sample, displaying the long-lasting incorporation of $CaCO_3$ into the matrix of CO_2-injected pastes. Most notably, the carbonated sample also contains broad amorphous humps at ~300–560 cm^{-1} and ~870–960 cm^{-1} which can be assigned to silica gel. These bands initially have a high normalized intensity in the first hour of hydration and decrease over time to negligible amounts by the ~10th hour. In contrast, reference samples contain no silica gel bands at these wavelengths throughout the 24 h experimental window.

Additionally, there are stark differences in the evolution of the CH peak at 355 cm^{-1} and the corresponding 3618 cm^{-1} hydroxide stretching peak (latter not shown) between the two sample types.

While reference spectra show gradual and consistent growth in CH crystals over time (as is expected in ordinary cement hydration), the average spectra of CO_2-activated samples contain no CH until the fifth hour of hydration, after which the portlandite peak grows explosively to reach a near-maximum intensity by hour 6. This strongly suggests an alternative hydration pathway in 1% CO_2-dosed samples that results in both the formation of a transient amorphous silica gel phase, as well as the delayed formation of CH.

To better understand these hydration differences, a third analytical technique—temporal peak evolution analysis—is used to identify the chemical and crystallographic nature of relevant phases. Namely, a MATLAB script was devised to calculate the position, width and intensity of the CH and silica gel peaks in the average spectra (centered around 355 cm^{-1} and ~460 cm^{-1}, respectively) by fitting each peak with a Gaussian distribution and deconvoluting their overlapping intensities. Figure 3B shows the evolution of each phase's deconvoluted and fitted peak, tracking the peak's amplitudes over 24 h (again normalized by belite as an internal standard).

In line with results displayed visually in the average spectra in Figure 3A, CH is present in the reference sample almost immediately after hydration begins, and its peak grows steadily until ~12 h, after which it maintains a relatively constant level. The CO_2-activated sample, on the other hand, contains no CH until ~4–5 h, after which the peak amplitude grows rapidly, briefly overtaking the reference sample before leveling off around ~8 h. The CH peak of reference samples was also observed to have a shifted position (x_0: 357.2 → 356.0 cm^{-1}) and broadened width (w: 17.6 → 19.0 cm^{-1}) in the early hours of hydration, supporting previous findings on the presence of DCH (disordered/nano-CH) as a precursor to CH [21]. Meanwhile, the fitted peak for silica gel is nonexistent in the reference sample. In the CO_2-activated sample, it initially has a high amplitude, then decreases steadily in the first 4–5 h, and finally reaches near-zero levels by ~8 h. However, the final amplitudes of both the fitted CH and silica gel peaks are nearly identical between the reference and carbonated samples after ~12 h.

This points toward a destabilizing effect of CO_2 mineralization during the early hours of hydration, particularly in the first 4–5 h for samples with 1% CO_2 addition. Importantly, the carbonate region at ~1086 cm^{-1} in the CO_2 sample also reaches its apex by the fifth hour in Figure 3A, correlating the changes in CH and silica gel to the same time frame as the crystallization of $CaCO_3$ from injected CO_2. Following this initial period, the system tries to correct for the effects of carbon mineralization by rapidly consuming silica gel and producing CH, bringing the levels of both phases to that of reference samples. This suggests a return to traditional hydration pathways after the initial effects of CO_2 injection and subsequent carbonate mineralization within the cement matrix.

3.3 | Spatial and Temporal Evolution of Phases With Correlation Functions Analysis

The basis spectra established in Figure 2 can also be used in CRM to spatially map the distribution of different phases by filtering Raman bitmaps for the characteristic peak positions of each phase. As such, mapping the scan areas used in spectral analysis in Section 3.2 can provide a framework for visually and quantitatively validating the effects of CO_2 injection on early-stage clinker hydration.

Phase maps for C_3S (green), CH (yellow), silica gel (gray), and carbonates (red) were combined to show the parallel dissolution of early-stage silica gel and precipitation of CH in CO_2-activated pathways, which are absent from traditional hydration (Figure 4A,B). Clinker hydration is evident in both the reference and 1% CO_2 phase maps, as green C_3S clusters gradually decrease over time; smaller particles hydrate more rapidly in the early hours, and only the largest alite (C_3S) clusters remain not fully hydrated by the 24th hour. In the reference sample (Figure 4A), small, sporadic regions of red carbonates are present but do not grow or change over 24 h, indicating they originate from the cement's intrinsic calcite content. By contrast, in the sample exposed to 1% CO_2, the carbonate regions expand noticeably within the first 5 h. This expansion demonstrates the mineralization of calcite from the injected CO_2, consistent with the observations in Figure 3A.

Figure 4A shows that reference samples follow traditional hydration pathways, where CH crystals appear almost immediately as C_3S reacts with water, and progressively increase to fill the matrix (alongside C–S–H). However, in 1% CO_2 samples, silica gel is both abundantly present and uniformly distributed across the entire sample area in the first hours of hydration (Figure 4B). At the same time, CH is missing entirely until Hours ~4–5, when large clusters appear and break up the silica gel network. This phase transformation continues at a rapid rate, with very little silica gel left by 7 h, and practically none at 10 h, while CH proliferates in concomitance with the silica gel consumption.

In addition to visually displaying the chemical interaction of different components, the phase maps of 1% CO_2 samples were also quantitatively analyzed using two-point correlation functions to characterize the distribution and spatial correlation between different phases [42]. Binarizing the maps of individual phases allowed computation of the volume fraction (Φ) of the scan area (100 μm × 100 μm) occupied by each phase over time (Figure 4C). Provided the binary phase maps, a MATLAB script was utilized to compute the characteristic cluster length (λ_c) and characteristic cross-phase distances (δ_x) between C_3S, CH, and silica gel. The cluster length is determined via the application of a two-point cluster function, which describes the probability that a randomly generated line segment of length r will have both ends in the same cluster of a given phase; the most probable outcome approximates the average diameter of the clusters of that phase (λ_c) in the sample area (Figure 4D). The cross-phase distance is instead found using a two-point cross-correlation function, which describes the probability of a randomly generated line segment of length r to have one end in a given phase, and the other end in different phase. The cross-phase distance (δ_x), representing the global maximum of this function, thus provides a measure of the average spatial distance between two different phases in the sample area (Figure 4E). Calculation of these three correlation measures (Φ, λ_c, and δ_x) from Raman phase maps closely follows the methodology established in previous work [16, 21].

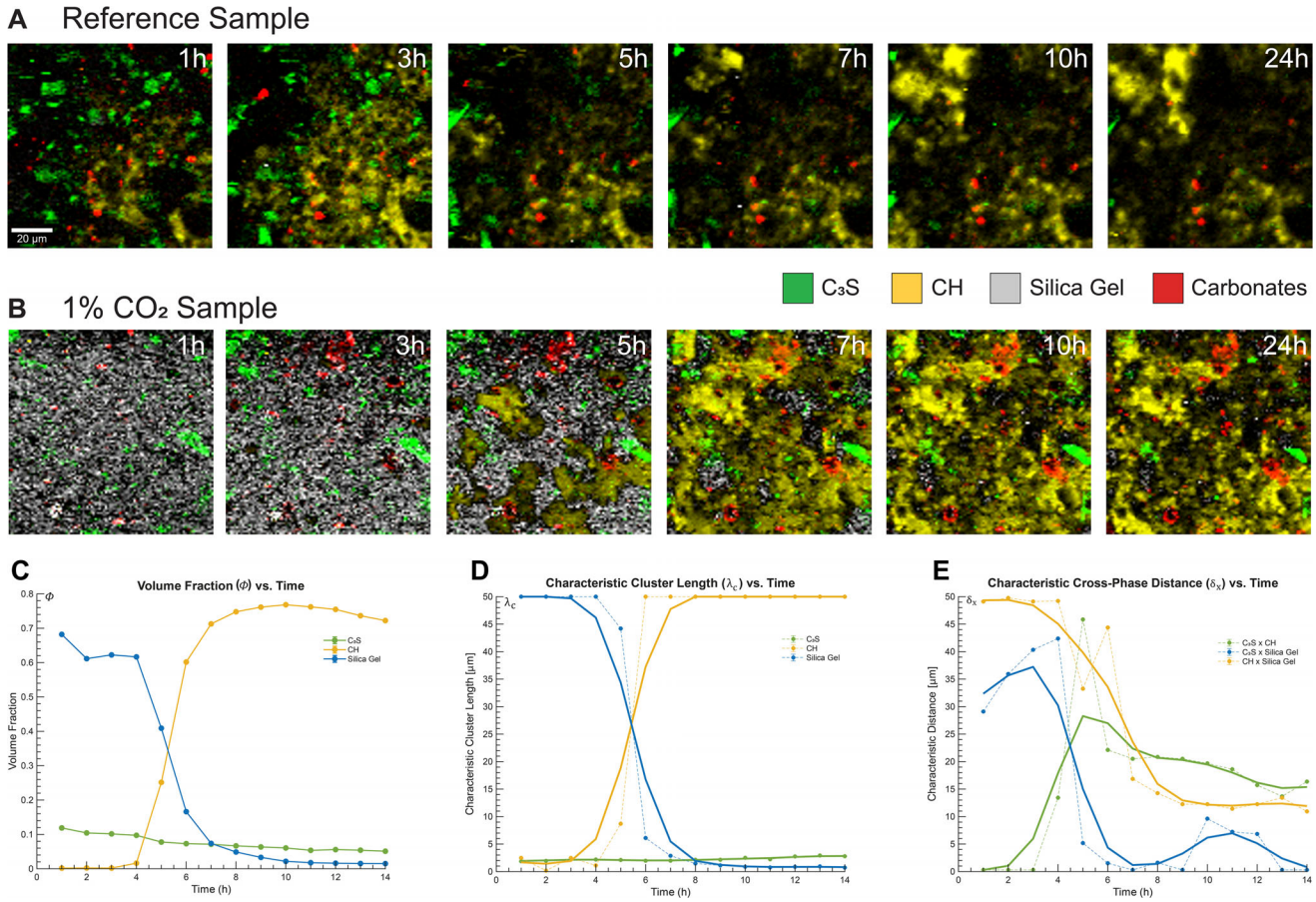

FIGURE 4 | Phase mapping and spatial analysis of hydrate and carbonate reaction products. Time- and space-resolved Raman maps illustrate the evolution of phases: (A) Reference Class G cement hydration compared to (B) samples with 1% CO_2 addition by mass. Key phases are highlighted: C_3S (green), CH (yellow), silica gel (gray), and carbonates (red). Correlation functions in panels (C–E) specifically analyze 1% CO_2 samples during early stages of hydration (1–14 h): (C) The volume fraction (Φ) of the main phases calculated from Raman maps of representative sample areas; (D) Characteristic cluster lengths (λ_c) of phases over time, determined via the application of a two-point cluster function; (E) Characteristic cross-phase distances (δ_x) between C_3S, CH, and silica gel during early hydration, determined using two-point cross-correlation functions. Solid lines in D and E represent fitted curves.

The volume fraction at each time step provides information on sample area composition and hydration kinetics. Figure 4C demonstrates that the dissolution of C_3S proceeds steadily in CO_2-activated samples in the first 14 h of hydration (constant decrease in Φ). Portlandite is nonexistent in the sample area in the first 4 h, after which it precipitates almost entirely between 4 and 8 h and then maintains a constant, high Φ value. Conversely, silica gel occupies ~65% of the sample area over the first 4 h, but sharply declines between 4 and 8 h to a near-zero Φ value. It is worth noting that the sum of Φ of all phases can potentially exceed 1.0 if Raman phases overlap. While the phase volume fraction (Φ) reported in Figure 4C from a 100 μm × 100 μm scan area represents local mesoscale distributions, at least three replicate samples were prepared and scanned with Raman spectroscopy to ensure that results are representative of the bulk material. As shown in Figure S1, the time evolution of the phase volume fraction of silica gel and CH is very similar across all samples, providing a robust approximation of the bulk phase distribution during early hydration.

The evolution of characteristic cluster length of the selected phases demonstrates the interconnectedness of the silica gel and CH, the former in the early hours of CO_2-injected samples, and the latter in later stages (Figure 4D). Note that the maximum distances considered in both cluster and cross-phase correlation analysis is half the sample dimension (50 μm). This limit ensures statistical validity by preventing artifacts that arise from boundary effects and insufficient sample overlap in a finite area. Since silica gel has a λ_c of 50 μm in the first 4 h of hydration, the phase is distributed across the sample area as a highly connected network, essentially comprising a single large cluster. Its rapid dissolution in Hours 4–8 breaks the silica gel into individual clusters scattered across the sample area, lowering the λ_c to zero. Portlandite shows the opposite trend, having an initial near-zero cluster length, which quickly spikes as CH precipitates to form an interconnected network with an average λ_c of 50 μm after 6–8 h of hydration. Both CH and silica gel particle size plateau after 8 h, suggesting a stabilization of the system following mineralization-induced changes to early-stage hydration kinetics. C_3S cluster size increases slightly over time, as smaller alite particles hydrate more quickly and larger ones remain in the matrix for longer.

While volume fraction and cluster length analysis describe trends in the amount and size of different phases, they do not capture the

interactions at phase boundaries. Cross-phase correlation helps reveal how these different phases precipitate and are spatially distributed relative to one another. Because no portlandite is present in the 1% CO_2 sample in the first 4 h, δ_x values for $C_3S \times$ CH and CH × silica gel in that time frame are mathematically undefined, yielding computational artifacts at the minimum (0 μm) and maximum (50 μm) limits of the plot, respectively. Once portlandite precipitates at ~5 h, the δ_x for $C_3S \times$ CH is 45.7 μm, showing that CH clusters nucleate far from clinker particles. As CH fills the pore space, δ_x stabilizes to 20.9 μm after 8 h of hydration. Because the cross-phase distance (δ_x) approximates the "center-to-center" distance between particles of one phase and particles of another, combining this information with the average particle radii ($\lambda_c/2$) can illuminate interaction fronts between phase surfaces. Considering the characteristic particle radii of alite (~2 μm) and CH (~25 μm) after 8 h, a δ_x of 20.9 μm indicates potential overlap between these phases, as can visually be seen in Figure 4B.

C_3S and silica gel are both present in the CO_2-activated sample from the start of hydration and initially have a cross-phase distance of 29.2 μm (Figure 4E). The δ_x grows to 42.6 μm by Hour 4, before dropping sharply to near-zero values during the rapid dissolution of silica gel. The large initial distance shows that silica gel, like CH, nucleates far from C_3S particles. This suggests a through-solution mechanism, where silicate groups from the clinker dissolve into the pore water and then precipitate to form silica gel far from the alite source. Since silica gel is spread throughout the sample area as early as 1 h, the increase in δ_x for $C_3S \times$ silica gel in the first 4 h is due to dissolution of small clinker particles (thus making C_3S more spread out) rather than a sign of the silica gel moving further away from clinker. Trace signals of silica gel (largely caused by noise in the Raman spectra in the 300–560 μm range) produce random variations in δ_x for $C_3S \times$ silica gel at later stages, even though actual silica gel is not present in the sample after ~10 h (Figure 4C). Once CH starts to form, the cross-phase distance for CH × silica gel is initially high (~40 μm) and rapidly decreases as the amorphous gel dissolves and CH appears in its place. The δ_x stabilizes around ~14 μm after 8 h rather than the expected ~0 μm, another artifact of trace Raman signals for other phases in the characteristic wavenumbers for silica gel.

The quantitative analysis plotted in Figure 4C–E is derived from the phase maps of the 1% CO_2 sample shown in Figure 4B for direct comparison. However, multiple samples were prepared and tested in the same manner using correlation function analysis, all of which confirmed the same altered hydration trends under CO_2 injection (see Figure S1).

3.4 | In Situ Observation and Thermodynamic Drivers of Pozzolanic Reactions

A key observation of this Raman analysis from all replicate samples is the emergence of three distinct stages of early-stage carbonation: *(1) Mineralization Stage (0–4 h)*: As CO_2 mineralizes, an interconnected network of silica gel is present throughout the sample, while calcium hydroxide is absent entirely; *(2) Transition Stage (4–8 h)*: Silica gel rapidly dissolves and CH concurrently precipitates into the resulting voids; *(3) Stabilization Stage (> 8 h)*: The volume fraction (Φ), cluster length (λ_c), and cross-phase distance (δ_x) of the phases all plateau, signaling that the system stabilizes as traditional hydration products form and the material sets.

Correlation function analysis particularly highlights the *Transition Stage* in CO_2-injected samples, characterized by large-scale consumption of silica gel and replacement with portlandite. However, to fully understand the reaction mechanism governing this transformation, the reaction front between the two phases was analyzed at higher resolution with Raman mapping between 4 and 6 h. The time lapse of these phases (Figure 5A) shows that the rapid dissolution of silica gel (gray) in this time frame is spatially coupled to the precipitation of CH (yellow), rather than occurring indiscriminately in the sample area. While Figure 4C,D confirms this rapid change in volume fraction and cluster length, cross-correlation analysis is limited in describing this phenomenon due to the large, connected phase networks in a relatively small sample area. Individual phase maps, however, show a near-perfect spatial anticorrelation ($r = -0.966$) between the two phases during this *Transition Stage* (Figure 5A).

Detailed inspection of individual precipitating calcium hydroxide particles reveals a distinct interfacial layer (dark gray) between the growing CH and the receding silica gel where neither phase is present (Figure 5B). Given the micron-level resolution of the collected scans (1 pixel = 1 μm), the lack of either phase is not merely an imaging artifact, but rather a unique third phase. Ranging from 1 to 7 μm in thickness around CH particles, this layer was observed in all samples with CO_2 addition.

This distinct interstitial phase is identified as an early-age pozzolanic form of calcium–silicate–hydrate, designated C–S–H* to distinguish its unique formation pathway from ordinary C–S–H produced during primary clinker hydration. Its formation at the reaction front between a known calcium source (CH) and a reactive silica source (amorphous silica gel) naturally points toward a localized pozzolanic reaction (Equation 3) with a calcium–silicate–hydrate as the expected product. The exact stoichiometry of the reaction in Equation (3) may change based on the Ca/Si ratio in the final C–S–H* product. The precipitation of this C–S–H* continues alongside the rapidly shifting reaction front during the *Transition Stage*. As CH grows, it consumes silica gel to produce C–S–H* at the interface between the two phases. This allows C–S–H* to proliferate alongside the CH at the reaction front until all of the silica gel is consumed.

$$3Ca(OH)_2 + 2SiO_2 + nH_2O \rightarrow (3CaO \cdot 2SiO_2 \cdot (n+3)\,H_2O) \quad (3)$$

This formation of pozzolanic C–S–H* from silica gel occurs in specific environmental conditions that favor its precipitation in CO_2-activated samples, as shown in isothermal calorimetry and pore solution pH measurements in Figure S2. The stability of the transient silica gel and the subsequent precipitation of C–S–H* are heavily dependent on the alkalinity of the pore solution. Upon the introduction of CO_2, the dissociation of carbonic acid rapidly consumes hydroxyl ions (OH^-), resulting in a suppressed initial pH of 12.58, compared to 13.07 in the reference system at 30 min of hydration (Figure S2B). This reduction in OH^- groups prevents the alkaline hydrolysis of Si–O–Si bonds, keeping the silica gel intact as an amorphous network during the *Mineralization Stage*. As clinker dissolution continues, the

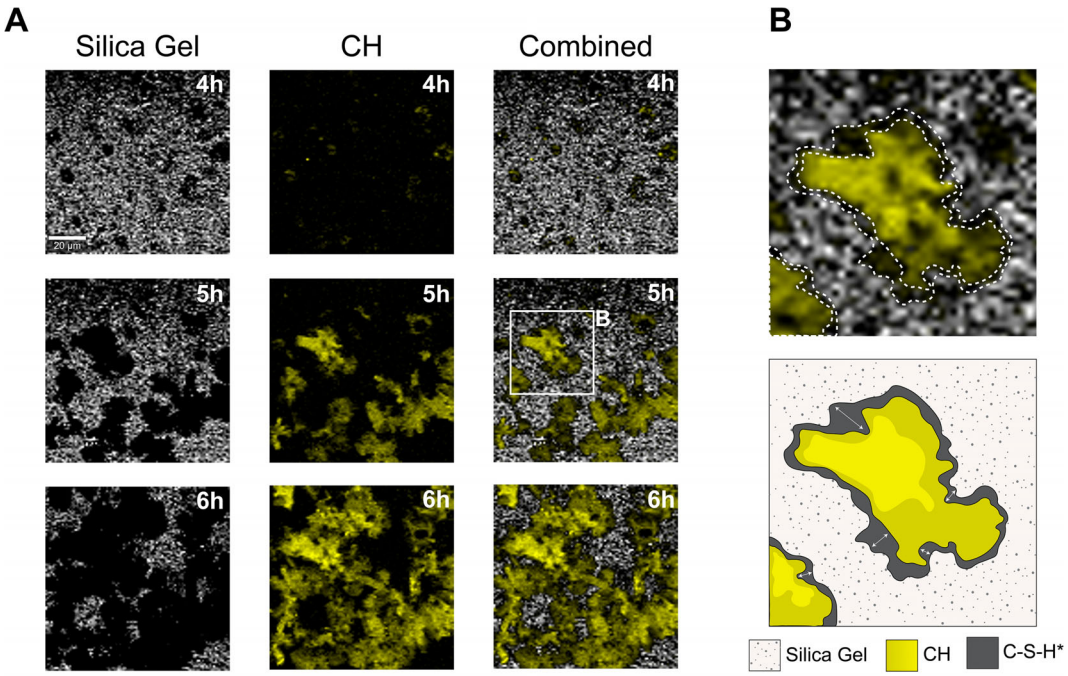

FIGURE 5 | In situ Raman mapping of 1% CO_2 samples reveals an interstitial phase during early hydration. (A) Between 4 and 6 h of hydration, silica gel (gray) rapidly dissolves from an interconnected network to sparse clusters. Simultaneously, CH forms in regions previously occupied by the silica gel, indicating a direct reaction at their interface. (B) A distinct interfacial layer between growing CH particles and dissolving silica gel is attributed to C–S–H* (dark gray), a pozzolanic C–S–H variant observed in samples with CO_2 mineralization.

1% CO_2 system experiences a steady recovery in pore solution alkalinity, ultimately matching the reference pH between 5 and 7 h (Figure S2B). This surge in pH allows for the hydrolysis of bonds in the silica network, destabilizing the transient gel. The resulting release of silicates, coinciding with the precipitation of CH observed in Figure 5, provides the thermodynamic trigger required for the rapid pozzolanic precipitation of the C–S–H* phase during the *Transition Stage*.

The kinetic footprint of this reaction is likewise captured by heat flow data in isothermal calorimetry (Figure S2A). Due to the formation of calcium carbonate and silica gel, CO_2-injected samples experience an elongated induction period that aligns with the *Mineralization Stage* observed in Raman maps during the first 4–5 h. However, the 1% CO_2 system also exhibits a noticeably higher baseline heat flow during this induction period. This elevated thermal output indicates rapid clinker dissolution to drive $CaCO_3$ precipitation, suggesting that the newly formed silica gel does not act as a passivating layer around clinker particles. Coinciding with the rise in pH and destabilization of the silica gel, the calorimetry curve of the CO_2-activated sample rapidly rises at ~5 h, marking the onset of the acceleration period. Although delayed compared to the reference sample, the acceleration period is marked by a curve with a sharper upward slope, as indicated by thermal markers in Figure S2A, suggesting a rapid burst of reaction activity during the *Transition Stage*. Importantly, the 1% CO_2 system displays a distinct double-peak during this delayed acceleration phase. The initial peak around 10 h of hydration reflects the intense, localized reaction occurring as the silica gel reacts with CH along a rapidly moving reaction front to produce C–S–H*. The second peak at 15 h indicates the stabilization of the pore chemistry and the resumption of standard clinker hydration. Despite the unique conditions supporting pozzolanic C–S–H* formation in samples with 1% CO_2 addition, the cumulative heat flow for both systems converges by 72 h, suggesting that the ultimate degree of cement hydration is not compromised.

3.5 | CO_2-Induced Hydration Pathway and Early Strength Development

The culmination of results from spectroscopic kinetics (Figure 3), quantitative microstructural evolution (Figure 4), and direct imaging of the reaction front (Figure 5) allows for the construction of a complete, novel hydration pathway for CO_2-activated cements shown in Figure 6. This schematic representation describes a mechanism whereby early-stage CO_2 injection reroutes conventional hydration, using a transient silica gel as a template to form a widely distributed, pozzolanic C–S–H* microstructure.

In traditional hydration, clinker's reaction with water rapidly produces amorphous portlandite (as evidenced by the DCH spectral peak broadening and shifting detailed in Section 3.2), which subsequently crystallizes into CH in the pore space (Figure 6A II). Concurrently, calcium and silicates from C_3S react with water to produce localized C–S–H that surrounds the alite particles (Figure 6A III). The formation of both products is almost instantaneous, and both continue expanding until the pore space is filled with a matrix of C–S–H gel with embedded CH crystals (Figure 6A IV). These two products are the backbone of concrete's strength, creating a fundamental framework in the material within 24 h, and a densified mature microstructure after

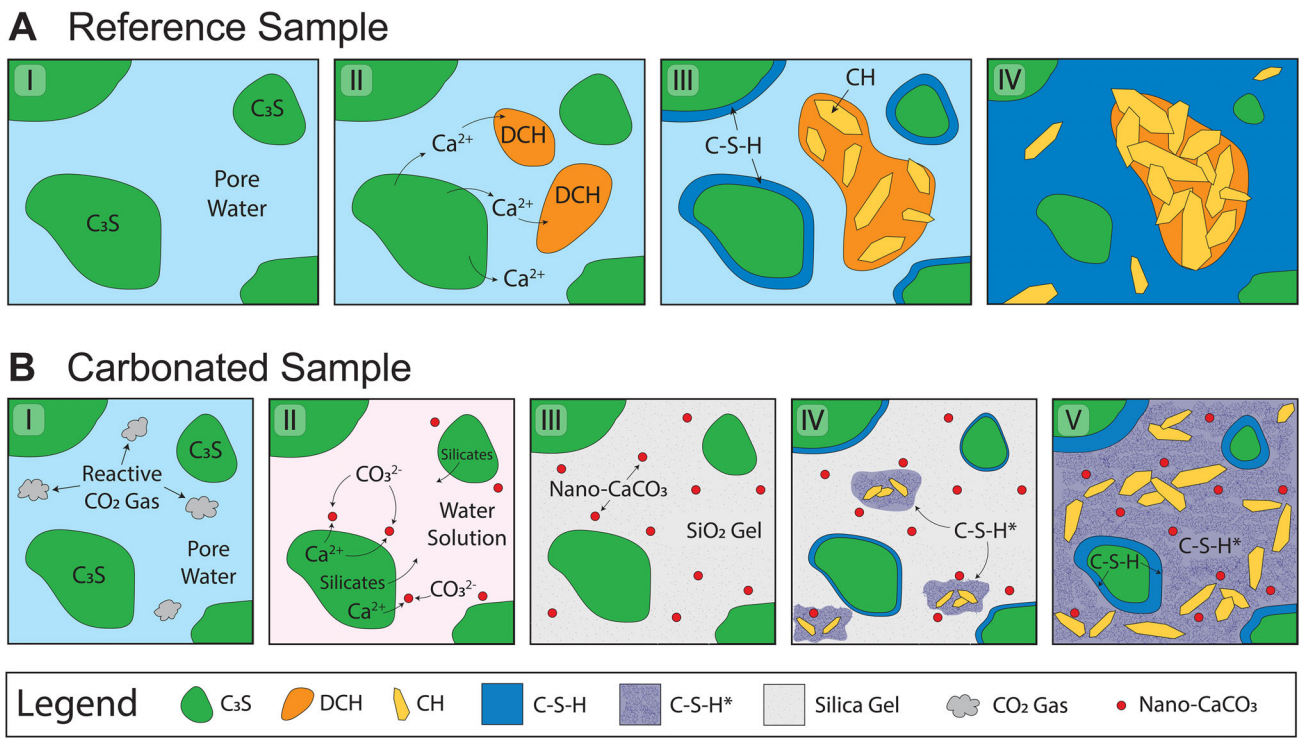

FIGURE 6 | Schematic representation comparing traditional early-stage cement hydration to an alternative pathway in which CO_2 mineralization forms a silica gel template. (A) In ordinary cement hydration, clinker dissolves in the matrix allowing early disordered CH (DCH) to form in pores (II). Over time, DCH converts to crystalline CH, while C–S–H forms around the C_3S clusters, rapidly expanding to eventually fill the pore space (III–IV). (B) In samples with CO_2 addition, the presence of abundant carbonate ions near hydration sites leads to the partial dissolution of clinker particles (II). The carbonate ions leach calcium from C_3S to form nano-$CaCO_3$ particles, while the resulting silica forms a reactive silica gel that rapidly spreads throughout the matrix (III). Once CO_2 is depleted, CH begins to form following traditional hydration pathways, and immediately reacts with the abundant silica gel to form pozzolanic C–S–H* not found in reference samples (IV). The widespread distribution of the silica gel allows it to act as a template for the formation of C–S–H* throughout the matrix, while the remaining C_3S particles still produce ordinary C–S–H localized around the hydration sites (V).

28 days [1, 43]. This pathway has been established in previous Raman investigations of OPC hydration, and confirmed here in the hydration of reference Oilwell Type G cement samples, both through the evolution of Raman spectra (Figure 3A) and Raman mapping (Figure 4A) [16, 21].

However, when CO_2 is introduced directly in the mixing process, it reacts with water to form carbonic acid (H_2CO_3). Driven by the highly alkaline pore solution, this acid subsequently undergoes rapid speciation, fully dissociating to yield hydrogen (H^+) and carbonate (CO_3^{2-}) ions (Equation 4). As clinker dissolves in water, the released Ca^{2+} ions react instantly with carbonate ions to produce nanocrystalline calcium carbonate ($CaCO_3$) according to Equations (1) and (2) (Figure 6B I–II). Because calcium carbonate possesses a significantly lower solubility product (K_{sp}) than portlandite (3.3×10^{-9} and 5.02×10^{-6}, respectively), the pore solution quickly reaches supersaturation with respect to $CaCO_3$. As a result, carbonate crystals precipitate rapidly in the cement matrix, effectively starving the competing hydration reaction of Ca^{2+} and lowering the saturation index of CH. This delays the formation of traditional hydration products until all CO_3^{2-} ions have been consumed. This is observed in the Raman spectra of CO_2-activated samples (Figure 3A), where an envelope of carbonate peaks at ~1080 cm^{-1} (containing calcite, aragonite, vaterite, and amorphous calcium carbonate) appears within the first hour of hydration and grows until Hour 5 (end of the *Mineralization Stage*). Raman mapping in Figure 4B also shows the red calcium carbonate crystals expanding spatially in the cement matrix during the first 5 h. Both the spectra and maps also show a steady level of $CaCO_3$ after 5 h owing to the high insolubility of calcium carbonate. This means that once formed, $CaCO_3$ crystals remain mineralized within the concrete matrix [16].

$$CO_2 + H_2O \rightarrow H_2CO_3 \rightarrow 2H^+ + CO_3^{2-} \quad (4)$$

The Raman investigation in this work suggests an additional mechanism for mechanical improvement, which originates from the creation of a transient silica gel that acts as a template for new C–S–H growth. When carbonate ions leach calcium from C_3S to produce calcite, the clinker dissolution also releases silicates. Without available calcium to form early-stage C–S–H directly around the surface of alite clusters, the silicates are instead forced to react with one another, polymerizing into silica chains that rapidly form an interconnected network (Figure 6B III). This reaction was observed to begin extremely rapidly upon hydration, with Raman spectra and maps showing the highest intensity of silica gel in the first hour. For example, Figure 3B shows that the mean amplitude of the silica gel band in Raman spectra of CO_2-activated samples is ~1.0 at 1 h, and drops to negligible amounts by Hour 8. Processing the Raman data at a higher temporal resolution (finer time intervals) revealed that the silica band grows to reach its maximum height within just 25–30 min of hydration, after which it starts to decrease to reach 1.0 by the end of the first hour. The proposed reaction mechanism also explains

the large initial cross-correlation distance between C_3S and silica gel in Figure 4E (δ_x of 29.2 μm), as the gel nucleates far from clinker particles in a through-solution process.

This rapid coprecipitation of the silica gel network with embedded $CaCO_3$ (Figure 6B III) effectively reduces the concentration of silicate and calcium ions below the saturation levels required for traditional CH and C–S–H formation during the *Mineralization Stage* (0–4 h). As a result, the CH peak at 355 cm^{-1} does not appear in 1% CO_2 samples until 5 h (Figure 3A), nor in Raman maps of the sample area until the same time frame (Figure 5A). Quantitative correlation function analysis confirms these observations with a near-perfect negative correlation between the volume fraction ($r = -0.988$) and cluster length ($r = -0.993$) of CH and silica gel in carbonated samples (Figure 4C,D). C–S–H follows the same pattern, with the average spectra of 1% CO_2 samples exhibiting very little change in the characteristic 660 cm^{-1} peak in the first 5 h (Figure 3A), excluding any small oscillations from the neighboring ferrite (C_4AF) peak at 725 cm^{-1}. At the same time, the amplitude of the primary C_3S peak at 828 cm^{-1} decreases slightly faster in the CO_2-injected sample, suggesting rapid clinker dissolution to supply the carbonate mineralization and silica gel formation reactions.

Once all carbonate ions from the injected CO_2 have been converted into calcium carbonate, the cement paste enters a *Transition Stage* (4–8 h). The undissolved clinker still available in the matrix continues hydrating, but the resulting silicates and calcium ions now fuel the regular hydration reaction. CH begins to precipitate and crystalize in the pore space, first evident in Raman spectra and maps after ~4–5 h (Figure 5A). As these delayed CH clusters form, they react with the widespread silica gel via a localized pozzolanic reaction to produce a distinct calcium–silicate–hydrate—C–S–H*—at the interface of the two phases. The precipitation of portlandite coincides with a rise in matrix pH driven by continued clinker hydration, which saturates the pore solution with OH^- ions to counteract the more acidic environment caused by carbonation (Figure S2B). This rising alkalinity, which converges with the pH of reference pastes by Hour 7, destabilizes the amorphous silica gel, whose Si–O–Si bonds are most stable in lower pH conditions. Consequently, the silica gel dissolves in this changing chemical environment, freeing its silicates to react with calcium to form C–S–H*. Likewise, oxygen and hydrogen atoms that were previously incorporated in the silica gel structure can now instead be used to form $Ca(OH)_2$.

This proposed series of reactions also provides a rationale for why the disappearance of silica gel and growth of CH is so fast and extensive during the *Transition Stage*. Once all CO_2 is mineralized, the precipitation of portlandite creates a cascade effect, where the increasing matrix pH promotes the dissolution of silica gel and subsequent production of more CH, which further increases the pH to destabilize silica gel, and so on. This chain reaction not only rapidly precipitates CH, but also creates a quickly moving reaction front between the CH and silica gel, allowing the resulting C–S–H* (Equation 3) to fill the sample matrix. In this manner, what starts off as a thin layer around individual CH clusters (Figures 5B and 6B IV) quickly expands to create a global C–S–H* network in the sample (Figure 6B V), utilizing the CO_2-induced silica gel as a template for its formation.

As the composite CH and C–S–H* fills the pore space, remaining clinker particles start to form a layer of ordinary C–S–H on their surface that gradually increases in thickness. This can be seen indirectly through the volume fraction of C_3S (Figure 4C), which continues to slowly decrease even after the *Transition Stage* is complete (> 8 h). This can also be observed from a mechanical perspective via the material's early stage compressive strength and setting behavior.

Tests conducted with a Vicat apparatus according to ASTM C191 [31] showed that 1% CO_2 injection accelerates the initial and final setting time of paste samples. Initial setting was achieved at 12 h 23 min in samples with CO_2 addition, compared to 13 h 32 min for reference samples. Likewise, final setting occurred at 22 h 45 min in the CO_2-injected samples, and was not observed at all in reference samples during the 24 h testing period at the 1.0 *w*/*c* ratio used in this study (see Figure S4A). At a macroscale, the early-age compressive strength of mortar cubes, determined in accordance with ASTM C109 [44], provides a direct measure of the microstructural development within the same time frame. As shown in Figure S4B, the CO_2 mix achieved a compressive strength of 7.39 MPa at 24 h, which represents a 13% increase over the 6.11 MPa measured for the reference mix. The precipitation of calcium carbonate and widespread distribution of C–S–H* physically bridges the gaps between clinker particles within the pore space much earlier in the reaction (Figure 4). This distributed microstructure explains the enhanced early-age mechanical performance and accelerated setting observed compared to conventional hydration.

Importantly, while CO_2-activated samples achieve higher early-stage mechanical performance due to these microstructural changes, they do not fully set by the end of the *Mineralization* and *Transition Stages*. With little to no precipitation of new CH or C–S–H* after the *Transition Stage*, the paste must rely on the formation of other products in this timeframe that allow it to fully harden and set—namely, ordinary C–S–H. This resumption of conventional hydration is supported by the distinct second calorimetry peak at ~15 h following the rapid pozzolanic formation of C–S–H* (Figure S2A). This suggests a return to traditional hydration pathways in the *Stabilization Stage* (> 8 h) after CO_2-injected pastes have accommodated other chemical priorities. The system must first fully mineralize the available CO_2 (0–4 h) and subsequently buffer the resulting chemical changes by transforming silica gel into C–S–H* and raising the pH (4–8 h) as shown in Figure S2B. Once this chemical stability is achieved, conventional hydration mechanisms are restored (Figure 6B V), allowing the slow formation of ordinary C–S–H from clinker that drives the material's final setting and long-term strength, mirroring the behavior of systems hydrating without CO_2 addition.

3.6 | Discussion

3.6.1 | Silica Gel Template as a Mechanism for Microstructural Enhancement

The in situ Raman investigation presented here reveals that early-stage CO_2 addition leads to the rapid formation of a reactive silica gel and its subsequent conversion into calcium–silicate–hydrate

via a distinct three-stage process outlined in Sections 3.4 and 3.5. In this process, the amorphous silica gel plays a central role by forming a widespread interconnected network in the matrix, providing a template for the formation of a similarly widely distributed C–S–H* phase. This templated mechanism provides a new chemomechanical framework for understanding how CO_2 utilization enhances cementitious material performance.

A key implication of this work is a reinterpretation of the role of nanocarbonates in early-stage strength development. Previous literature has in some cases attributed the mechanical benefits of CO_2 addition to the densification of the microstructure by nanocrystalline $CaCO_3$ [47–49], or has hypothesized that these carbonate particles act as nucleation sites to "seed" C–S–H growth based on the spatial colocation of the two phases [16, 50]. The direct imaging of the reaction front in Figure 5 shows that C–S–H* forms at the interface of dissolving silica gel and precipitating portlandite, not on carbonate surfaces as would be expected under prior hypotheses. The chemical stability of $CaCO_3$ and its unchanging presence in Raman spectra over time also suggests that the carbonates themselves do not react to form C–S–H. Instead, the $CaCO_3$ crystals are spatially colocated with the final C–S–H* because they are passively embedded within the true reactive precursor—the silica gel template. When CO_2 leaches calcium from clinker, the amorphous gel fills the matrix around the nanocarbonates and is then replaced by C–S–H*.

The formation of C–S–H* via this templated pathway also provides a compelling explanation for the well-documented enhanced early-age strength in cementitious materials with CO_2 addition [26, 51–53]. Since the reactive silica gel template is formed in a through-solution mechanism, it spreads throughout the material during the early stages of hydration. By forming throughout the matrix wherever the silica gel template exists, C–S–H* creates a more homogenous and interconnected binder at a much earlier stage than is possible through conventional hydration, where ordinary C–S–H forms locally on the surface of clinker grains.

Beyond its widespread distribution, the nature of the pozzolanic C–S–H* formed from a highly polymerized silica gel template may also be intrinsically different from ordinary C–S–H. It is well established that a higher degree of silicate polymerization (lower Ca/Si ratio) in C–S–H correlates directly with increased stiffness and improved mechanical performance [54–56]. The formation of C–S–H* from a silicate-rich gel precursor strongly suggests it may have a higher mean silicate chain length than ordinary C–S–H formed through clinker dissolution, resulting in a more dense and less porous microstructure. Given that C–S–H and C–S–H* share a very similar general structure, it is difficult to definitively distinguish the two in Raman spectra, but differences in the degree of polymerization between reference and 1% CO_2 samples can still be observed. Deconvolution analysis of the C–S–H regions of Raman spectra in Figure 3A revealed that samples with CO_2 addition contained a greater relative concentration of higher Q_n silicate species, indicating a more cross-linked silicate network.

Evidence for this enhanced polymerization is observed across the temporal evolution of the silicate phases, beginning with the lower order Q_1 species at 897 cm^{-1} (Figure 2), representing silica dimers and chain-ends bonded to only one other silicate. While reference samples exhibit a steady, gradual decline in this Q_1 signal over the first 15 h of hydration, samples with 1% CO_2 demonstrate a much more rapid depletion in which the relative intensity of the Q_1 peak drops sharply within the first hour and diminishes to near-zero amplitude by Hours 4–5. This suggests that in samples with CO_2, these low-order silicates are rapidly polymerizing into higher order structures, coinciding directly with the onset of the Transition Stage detailed in Sections 3.4 and 3.5. Alongside this rapid Q_1 decline, we observe a distinct evolution in the Q_2 phase (a silicate bonded to two other silicates), characterized by the primary C–S–H Raman peak at 660 cm^{-1} (Figure 2). While reference samples show steady growth in this 660 cm^{-1} peak from the onset of hydration (Figure 3A), there is no considerable growth until after the first 5 h in carbonated specimens. Instead, the 1% CO_2 samples experience the vast majority of their Q_2 peak development between Hours 5 and 10, corresponding strongly with the duration of the Transition Stage. Conversely, preliminary observation of the 1% CO_2 spectra suggests an increase in intensity in the region associated with Q_3 C–S–H (1064 cm^{-1}) during the earliest stages of hydration (Figure 3A) [21]. Although the Q_3 region overlaps with the main carbonate peak at 1086 cm^{-1}, deconvolution analysis resulted in two distinct peaks for Q_3 C–S–H and carbonates in the CO_2-injected samples, while only the carbonate peak was present in the reference. This suggests that samples with CO_2 injection may first produce a more highly polymerized C–S–H* (rich in Q_3 and deficient in early Q_1/Q_2 species), before transitioning to producing standard C–S–H dominated by Q_2 phases in later stages, in line with the proposed hydration mechanism in Figure 6B.

These results indicate that the templated silica gel pathway may produce not only a more distributed binder network, but also a more highly polymerized, and thus potentially mechanically superior, binder in the form of C–S–H*. The accelerated development of this network is complemented by Vicat test results performed in this study, which showed the carbonated samples fully setting before 24 h, while reference samples only underwent initial setting in the same time frame (see Figure S4A). Together with its matrix-wide distribution, this microstructural densification of C–S–H* is likely a primary driver of the early-stage compressive strength gain in carbonated systems observed in literature [52, 53].

3.6.2 | Dosage-Dependent Effects

The results presented here have largely focused on systems with 1% CO_2 addition (wt% of cement), but it is well established that the effects of early-stage CO_2 activation are dosage-dependent in cementitious materials [51, 53, 57, 58]. As such, preliminary tests were also conducted on samples with 0.1% and 0.3% CO_2 injection with the same 24 h in situ Raman procedure outlined in Section 2. Analysis of these lower CO_2 dosages (Figure S3) reveals that the silica gel-templated pathway summarized in Figure 6B still holds true at lower dosages of CO_2. A distinct widespread silica gel still formed in these samples during the *Mineralization Stage*, and was replaced by widespread CH and C–S–H* in the *Transition Stage* before the matrix stabilized to produce ordinary hydration products.

However, the reaction kinetics governing the timing of these stages displayed a clear dosage-dependent effect. While the 1% CO_2 samples showed the highest concentration of silica gel in the first hour followed by a drastic conversion of the gel into C–S–H* between 4 and 8 h, the same reactions appeared delayed with lower levels of CO_2 injection. The silica gel grew steadily under lower dosages, reaching its maximum intensity in ~6 h in samples with 0.3% CO_2, and ~8 h in samples with 0.1% CO_2, before decreasing in both samples to produce pozzolanic C–S–H* (Figure S3). This points to a dose-dependent relationship where higher levels of CO_2 addition lead to more rapid silica gel formation and subsequent consumption. This is likely influenced by the concentration of carbonate ions in the matrix at different dosages, which dictates the extent to which the carbonation-driven pathway supersedes traditional hydration. However, the exact mechanism governing these reaction kinetics is outside the scope of this work and warrants further investigation.

This dose-dependent relationship also raises critical questions about how this novel hydration pathway behaves at higher CO_2 dosages. A key consideration is whether all available clinker would be consumed in the *Mineralization Stage* to form calcium carbonate and silica gel if abundant CO_2 is added to the early-age system. Such a scenario would halt the reaction at the stage shown in panel III of Figure 6B. This would prevent the formation of portlandite and its subsequent conversion of silica gel to strength-enhancing C–S–H*, negating the mechanical benefits explained earlier. Based on the mineralogical composition of the Oilwell cement used in this work (Table S2), the stoichiometric limit of CO_2 required to completely carbonate all the calcium from the silicate phases (C_3S and C_2S) is approximately 44.7% by weight of cement. Therefore, a key challenge moving forward is to identify an optimal dosage that maximizes the formation of the templated C–S–H* microstructure while still producing enough traditional hydration products to ensure long-term strength and a chemically stable alkaline environment.

3.6.3 | Future Work and Implications

The core of this study centered on Raman spectroscopy, as its unique ability to detect amorphous phases was essential for capturing the in situ formation and consumption of the transient silica gel. While this specialized approach provided novel chemical insights, existing limitations should be acknowledged to contextualize the findings and suggest avenues for future work. First, while the proposed chemical properties of C–S–H*, such as its higher silicate polymerization, were inferred from the Raman data, further research could help corroborate these results with other techniques. While conducting solid-state NMR for quantitative *Q*-phase determination could provide direct validation, traditional SEM-EDS mapping of local Ca/Si ratios is physically precluded here because the high water-to-cement ratio ($w/c = 1.0$) used in this work prevents the samples from sufficiently hardening within the 24 h testing period to allow for surface polishing. Additionally, while this work was specifically focused on early-stage hydration pathways, expanding the scope beyond the initial 24 h could help explore the stability of the reported C–S–H* phase, determining whether it remains a structurally distinct binder or acts as a transient intermediate that evolves toward conventional C–S–H during long-term clinker dissolution.

Furthermore, this investigation was conducted on a simplified cement paste system. Translating these insights to mortar or concrete will require further work, as the introduction of aggregates creates complex interfacial zones and the potential for alkali-silica reactions with the silica gel. Finally, although this study was primarily focused on elucidating novel chemical pathways, a complete chemomechanical understanding requires further mechanical investigation at both the micro- and macroscales. In this work, Vicat measurements and 24 h compression tests provided preliminary insights into the material's early-stage strength and setting behavior. However, complimentary compression and indentation tests at both early and late stages of hydration would be essential to directly measure the properties of the pozzolanic C–S–H* phase itself and definitively link the observed microstructural changes to large-scale performance.

Despite these open questions, the present findings have significant implications for the industrial application of CO_2 utilization technologies. Namely, the discovery that calcium carbonate crystals do not act as reactive nucleation sites for C–S–H, but rather as passive inclusions in the reactive silica gel, confirms that the mineralized CO_2 is permanently sequestered within the matrix. This validates CO_2 addition during mixing as a viable CCUS strategy to help the cement and concrete industry meet its climate goals. However, this work also underscores the importance of carefully optimizing the CO_2 dosage to balance the beneficial effects of the templated C–S–H* pathway while ensuring the material can return to traditional hydration to achieve proper long-term strength and chemical stability.

4 | Conclusion

The in situ Raman microspectroscopy investigation reported here conclusively demonstrates that early-age CO_2 injection fundamentally reroutes the chemical pathways of cement hydration by introducing a transient, reactive silica gel phase. This gel forms as a direct consequence of clinker dissolution under altered pore solution conditions induced by dissolved CO_2, which preferentially sequesters calcium ions into carbonate nanoparticles, leaving silicate species to polymerize into a widespread amorphous network. The critical finding is that this silica gel is not a terminal product but a reactive template. Its subsequent dissolution during the *Transition Stage* (4–8 h) is spatially and temporally coupled with the delayed precipitation of portlandite, at whose interface a pozzolanic C–S–H* phase forms. This mechanism is quantitatively validated by the observed anticorrelation in phase volume fractions, providing the first direct experimental evidence of a templated microstructural evolution in CO_2-activated cement.

These results lead to the conclusion that the mechanical enhancement observed in CO_2-activated cementitious systems is not solely attributable to the pore-filling effect of nanocarbonates but is significantly driven by this alteration of the hydration sequence. The silica gel-mediated pathway produces a more homogeneous and potentially more robust C–S–H* microstructure throughout the matrix, as opposed to the conventional C–S–H that forms

primarily around clinker particles in early-stage hydration. This work therefore establishes a new chemomechanical framework for understanding CO_2 utilization, positioning the amorphous silica gel as a critical intermediate phase governing performance. Consequently, optimizing CO_2 utilization technologies should focus not only on the degree of carbonate formation but also on controlling the kinetics of silica gel generation and consumption to engineer desired microstructures and final material properties.

Acknowledgments

We would like to thank the MIT Concrete Sustainability Hub (MIT CSHub) team for continuous support of this research. The authors gratefully acknowledge the reviewers for their time, effort, and constructive feedback, which have helped improve the quality of this manuscript.

Funding

The authors have nothing to report.

Data Availability Statement

Data sets generated during the current study are available from the corresponding author upon reasonable request.

References

1. P. K. Mehta, *Concrete: Microstructure, Properties, and Materials*, 4th ed. (McGraw-Hill Education, 2014).

2. L. Barcelo, J. Kline, G. Walenta, and E. Gartner, "Cement and Carbon Emissions," *Materials and Structures* 47, no. 6 (2014): 1055–1065, https://doi.org/10.1617/s11527-013-0114-5.

3. S. A. Miller and F. C. Moore, "Climate and Health Damages From Global Concrete Production," *Nature Climate Change* 10, no. 5 (2020): 439–443, https://doi.org/10.1038/s41558-020-0733-0.

4. IEA and WBCSD, *Technology Roadmap: Low-Carbon Transition in the Cement Industry* (OECD/IEA and WBCSD, 2018).

5. CEMBUREAU, *Cementing the European Green Deal* (European Cement Association, 2020).

6. Global Cement and Concrete Association, *Concrete Future—The GCCA 2050 Cement and Concrete Industry Roadmap for Net Zero Concrete* (Global Cement and Concrete Association, 2021).

7. Portland Cement Association, *Roadmap to Carbon Neutrality* (Portland Cement Association, 2021).

8. J. Monteiro and S. Roussanaly, "CCUS Scenarios for the Cement Industry: Is CO_2 Utilization Feasible?," *Journal of CO2 Utilization* 61 (2022): 102015, https://doi.org/10.1016/j.jcou.2022.102015.

9. M. Hanifa, R. Agarwal, U. Sharma, P. C. Thapliyal, and L. P. Singh, "A Review on CO_2 Capture and Sequestration in the Construction Industry: Emerging Approaches and Commercialised Technologies," *Journal of CO2 Utilization* 67 (2023): 102292, https://doi.org/10.1016/j.jcou.2022.102292.

10. S. Danieli, J. S. A. Neto, E. G. Soares, T. F. Oliveira, B. L. F. Brito, and A. P. Kirchheim, "Shaping a Sustainable Path: Exploring Opportunities and Challenges in Carbon Capture and Utilization in Cement and Concrete Industry," *Cement* 19 (2025): 100135, https://doi.org/10.1016/j.cement.2025.100135.

11. J. G. Driver, E. Bernard, P. Patrizio, P. S. Fennell, K. Scrivener, and R. J. Myers, "Global Decarbonization Potential of CO_2 Mineralization in Concrete Materials," *Proceedings of the National Academy of Sciences* 121, no. 29 (2024): e2313475121, https://doi.org/10.1073/pnas.2313475121.

12. J. F. Young, R. L. Berger, and J. Breese, "Accelerated Curing of Compacted Calcium Silicate Mortars on Exposure to CO_2," *Journal of the American Ceramic Society* 57, no. 9 (1974): 394–397, https://doi.org/10.1111/j.1151-2916.1974.tb11420.x.

13. S. Monkman, Y. Sargam, O. Naboka, and B. Lothenbach, "Early Age Impacts of CO_2 Activation on the Tricalcium Silicate and Cement Systems," *Journal of CO2 Utilization* 65 (2022): 102254, https://doi.org/10.1016/j.jcou.2022.102254.

14. S. Monkman, P. Kenward, and G. Dipple, "Physicochemical Impacts of In-Situ Mineralized $CaCO_3$ on Very Early Hydration of Cement at Two Temperatures," *ACS Sustainable Chemistry & Engineering* 11, no. 16 (2023): 6261–6271, https://doi.org/10.1021/acssuschemeng.2c07480.

15. S. Monkman, B. E. J. Lee, K. Grandfield, M. MacDonald, and L. Raki, "The Impacts of In-Situ Carbonate Seeding on the Early Hydration of Tricalcium Silicate," *Cement and Concrete Research* 136 (2020): 106179, https://doi.org/10.1016/j.cemconres.2020.106179.

16. D. Stefaniuk, M. Hajduczek, J. C. Weaver, F. J. Ulm, and A. Masic, "Step Toward Concrete Carbon Neutrality," *PNAS Nexus* 2, no. 3 (2023): pgad052, https://doi.org/10.1093/pnasnexus/pgad052.

17. Y. Sargam, S. Monkman, and V. Chaudhari, "CO_2-injected Cement Paste: Insights Into Microstructural and Chemo-Mechanical Changes," *Journal of Sustainable Cement-Based Materials* 15, no. 1 (2025): 1–14, https://doi.org/10.1080/21650373.2025.2565293.

18. A. M. Neville and J. J. Brooks, *Concrete Technology*, 2nd ed. (Prentice Hall, 2010).

19. X. Cong and R. J. Kirkpatrick, "29Si MAS NMR Study of the Structure of Calcium Silicate Hydrate," *Advanced Cement Based Materials* 3, no. 3–4 (1996): 144–156, https://doi.org/10.1016/S1065-7355(96)90046-2.

20. R. J. Kirkpatrick, J. L. Yarger, P. F. McMillan, Y. Ping, and X. Cong, "Raman Spectroscopy of C-S-H, Tobermorite, and Jennite," *Advanced Cement Based Materials* 5, no. 3–4 (1997): 93–99, https://doi.org/10.1016/S1065-7355(97)00001-1.

21. H.-C. Loh, H.-J. Kim, F.-J. Ulm, and A. Masic, "Time-Space-Resolved Chemical Deconvolution of Cementitious Colloidal Systems Using Raman Spectroscopy," *Langmuir* 37, no. 23 (2021): 7019–7031, https://doi.org/10.1021/acs.langmuir.1c00609.

22. S. Srivastava and N. Garg, "Tracking Spatiotemporal Evolution of Cementitious Carbonation via Raman Imaging," *Journal of Raman Spectroscopy* 54, no. 4 (2023): 414–425, https://doi.org/10.1002/jrs.6483.

23. K. Garbev, P. Stemmermann, L. Black, C. Breen, J. Yarwood, and B. Gasharova, "Structural Features of C–S–H(I) and Its Carbonation in Air—A Raman Spectroscopic Study. Part I: Fresh Phases," *Journal of the American Ceramic Society* 90, no. 3 (2007): 900–907, https://doi.org/10.1111/j.1551-2916.2006.01428.x.

24. L. Black, C. Breen, J. Yarwood, K. Garbev, P. Stemmermann, and B. Gasharova, "Structural Features of C–S–H(I) and Its Carbonation in Air—A Raman Spectroscopic Study. Part II: Carbonated Phases," *Journal of the American Ceramic Society* 90, no. 3 (2007): 908–917, https://doi.org/10.1111/j.1551-2916.2006.01429.x.

25. H. Liu, H. Kaya, Y. Lin, A. Ogrinc, and S. H. Kim, "Vibrational Spectroscopy Analysis of Silica and Silicate Glass Networks," *Journal of the American Ceramic Society* 105, no. 4 (2022): 2355–2384, https://doi.org/10.1111/jace.18206.

26. S. Monkman, P. A. Kenward, G. Dipple, M. MacDonald, and M. Raudsepp, "Activation of Cement Hydration With Carbon Dioxide," *Journal of Sustainable Cement-Based Materials* 7, no. 3 (2018): 160–181, https://doi.org/10.1080/21650373.2018.1443854.

27. P. T. Durdziński, M. Ben Haha, M. Zajac, and K. L. Scrivener, "Phase Assemblage of Composite Cements," *Cement and Concrete Research* 99 (2017): 172–182, https://doi.org/10.1016/j.cemconres.2017.05.009.

28. M. Saillio, V. Baroghel-Bouny, M. Bertin, S. Pradelle, and J. Vincent, "Phase Assemblage of Cement Pastes With SCM at Different Ages," *Construction and Building Materials* 224 (2019): 144–157, https://doi.org/10.1016/j.conbuildmat.2019.07.059.

29. A. Jagličić, T. Gädt, and M. Hofmann, "Automatic and Simple: How to Analyze Isothermal Calorimetry Data of Cement Hydration Quantitatively," *Journal of Thermal Analysis and Calorimetry* 150, no. 8 (2025): 5971–5980, https://doi.org/10.1007/s10973-025-14162-3.

30. C09 Committee, Practice for Measuring Hydration Kinetics of Hydraulic Cementitious Mixtures Using Isothermal Calorimetry (C09 Committee, n.d.), https://doi.org/10.1520/C1679-22.

31. C01 Committee, ASTM C191-21 Test Methods for Time of Setting of Hydraulic Cement by Vicat Needle (C01 Committee, n.d.), https://doi.org/10.1520/C0191-21.

32. European Committee for Standardization, EN 196-1:2016. Methods of *Testing Cement—Part 1: Determination of Strength* (European Committee for Standardization, 2016).

33. C01 Committee, ASTM C305-20 Practice for Mechanical Mixing of Hydraulic Cement Pastes and Mortars of Plastic Consistency (C01 Committee, 2020), https://doi.org/10.1520/C0305-20.

34. C09 Committee, ASTM C494/C494M-24 Specification for Chemical Admixtures for Concrete (C09 Committee, 2024), https://doi.org/10.1520/C0494_C0494M-24.

35. J. Higl, M. Köhler, and M. Lindén, "Confocal Raman Microscopy as a Non-Destructive Tool to Study Microstructure of Hydrating Cementitious Materials," *Cement and Concrete Research* 88 (2016): 136–143, https://doi.org/10.1016/j.cemconres.2016.07.005.

36. N. Prieto-Taboada, O. Gómez-Laserna, I. Martínez-Arkarazo, M. Á. Olazabal, and J. M. Madariaga, "Raman Spectra of the Different Phases in the $CaSO_4$–H_2O System," *Analytical Chemistry* 86, no. 20 (2014): 10131–10137, https://doi.org/10.1021/ac501932f.

37. G. Renaudin, R. Segni, D. Mentel, J.-M. Nedelec, F. Leroux, and C. Taviot-Gueho, "A Raman Study of the Sulfated Cement Hydrates: Ettringite and Monosulfoaluminate," *Journal of Advanced Concrete Technology* 5, no. 3 (2007): 299–312, https://doi.org/10.3151/jact.5.299.

38. L. Black, C. Breen, J. Yarwood, J. Phipps, and G. Maitland, "*In Situ* Raman Analysis of Hydrating C_3 A and C_4 AF Pastes in Presence and Absence of Sulphate," *Advances in Applied Ceramics* 105, no. 4 (2006): 209–216, https://doi.org/10.1179/174367606x120179.

39. V. Timón, D. Torrens-Martin, L. J. Fernández-Carrasco, and S. Martínez-Ramírez, "Infrared and Raman Vibrational Modelling of β-C2S and C3S Compounds," *Cement and Concrete Research* 169 (2023): 107162, https://doi.org/10.1016/j.cemconres.2023.107162.

40. A. E. Murphy, R. S. Jakubek, A. Steele, M. D. Fries, and M. Glamoclija, "Raman Spectroscopy Provides Insight Into Carbonate Rock Fabric Based on Calcite and Dolomite Crystal Orientation," *Journal of Raman Spectroscopy* 52, no. 6 (2021): 1155–1166, https://doi.org/10.1002/jrs.6097.

41. Y. Yue, J. Wang, and Y. Bai, "Tracing the Status of Silica Fume in Cementitious Materials Subjected to Deterioration Mechanisms With Raman Microscope," *Materials* 15, no. 15 (2022): 5195, https://doi.org/10.3390/ma15155195.

42. S. Torquato, "Microstructure Characterization and Bulk Properties of Disordered Two-Phase Media," *Journal of Statistical Physics* 45, no. 5–6 (1986): 843–873, https://doi.org/10.1007/BF01020577.

43. A. M. Neville, *Properties of Concrete*, 5th ed. (Pearson, 2011).

44. C01 Committee, ASTM C109 /C109M-16a Test Method for Compressive Strength of Hydraulic Cement Mortars (Using 2-in. or [50-mm] Cube Specimens) (C01 Committee, 2020), https://doi.org/10.1520/C0109_C0109M-16A.

45. P. Chindaprasirt and S. Rukzon, "Pore Structure Changes of Blended Cement Pastes Containing Fly Ash, Rice Husk Ash, and Palm Oil Fuel Ash Caused by Carbonation," *Journal of Materials in Civil Engineering* 21, no. 11 (2009): 666–671, https://doi.org/10.1061/(ASCE)0899-1561(2009)21:11(666).

46. Z. He, X. Shao, and X. Chen, "Effect of Carbonation Treatment on the Strength and CO_2 Uptake Rate of Composite Cementitious Material With a High Steel Slag Powder Content," *Materials* 16, no. 18 (2023): 6204, https://doi.org/10.3390/ma16186204.

47. A. Padmalal, K. Kulkarni, P. Rawat, and H. Sugandhini, "Efficacy of Accelerated Carbonation Curing and Its Influence on the Strength Development of Concrete," *Buildings* 14, no. 8 (2024): 2573, https://doi.org/10.3390/buildings14082573.

48. X. Xian, D. Zhang, H. Lin, and Y. Shao, "Ambient Pressure Carbonation Curing of Reinforced Concrete for CO_2 Utilization and Corrosion Resistance," *Journal of CO2 Utilization* 56 (2022): 101861, https://doi.org/10.1016/j.jcou.2021.101861.

49. M. Arandigoyen, B. Bicer-Simsir, J. I. Alvarez, and D. A. Lange, "Variation of Microstructure With Carbonation in Lime and Blended Pastes," *Applied Surface Science* 252, no. 20 (2006): 7562–7571, https://doi.org/10.1016/j.apsusc.2005.09.007.

50. Q. Luo, Y. Bai, Z. Li, X. Zhang, and M. Wu, "The Impact of Forced Early-Age Carbonation on the Hydration of Cementitious Materials," *Construction and Building Materials* 451 (2024): 138781, https://doi.org/10.1016/j.conbuildmat.2024.138781.

51. S. Monkman, M. MacDonald, R. D. Hooton, and P. Sandberg, "Properties and Durability of Concrete Produced Using CO_2 as an Accelerating Admixture," *Cement and Concrete Composites* 74 (2016): 218–224, https://doi.org/10.1016/j.cemconcomp.2016.10.007.

52. S. Zhang, Q. Yuan, J. Ni, C. Shi, K. Zheng, and J. Tan, "Study of CO_2 Injection Timing Within the Mixing Process of Ready-Mix Concrete for Win–Win Improvements of Mechanical Properties and CO_2 Sequestration," *ACS Sustainable Chemistry & Engineering* 12, no. 4 (2024): 1480–1492, https://doi.org/10.1021/acssuschemeng.3c05896.

53. S. Luo, M.-Z. Guo, and T.-C. Ling, "Modification of Early-Age Microstructure and Enhanced Mechanical Properties of Cement Paste via Injecting Low-Dose CO_2 at Fresh Stage," *Construction and Building Materials* 438 (2024): 137284, https://doi.org/10.1016/j.conbuildmat.2024.137284.

54. F. Pelisser, P. J. P. Gleize, and A. Mikowski, "Effect of the Ca/Si Molar Ratio on the Micro/Nanomechanical Properties of Synthetic C-S-H Measured by Nanoindentation," *Journal of Physical Chemistry C* 116, no. 32 (2012): 17219–17227, https://doi.org/10.1021/jp302240c.

55. J. J. Kim, E. M. Foley, and M. M. Reda Taha, "Nano-Mechanical Characterization of Synthetic Calcium–Silicate–Hydrate (C–S–H) With Varying CaO/SiO_2 Mixture Ratios," *Cement and Concrete Composites* 36 (2013): 65–70, https://doi.org/10.1016/j.cemconcomp.2012.10.001.

56. J. Wang, Z. Hu, Y. Chen, et al., "Effect of Ca/Si and Al/Si on Micromechanical Properties of C(-A)-S-H," *Cement and Concrete Research* 157 (2022): 106811, https://doi.org/10.1016/j.cemconres.2022.106811.

57. S. Monkman, Y. Sargam, and L. Raki, "Comparing the Effects of In-Situ Nano-Calcite Development and Ex-Situ Nano-Calcite Addition on Cement Hydration," *Construction and Building Materials* 321 (2022): 126369, https://doi.org/10.1016/j.conbuildmat.2022.126369.

58. X. Xian, C. Logan, and Y. Shao, "Dimensional Stability of Cement Paste and Concrete Subject to Early-Age Carbonation Curing," *Materials and Structures* 55, no. 3 (2022): 94, https://doi.org/10.1617/s11527-022-01926-8.

Supporting Information

Additional supporting information can be found online in the Supporting Information section.

Supporting File: jace70825-sup-0001-SuppMat.docx.